

Cr, Mo and W alloying additions in Ni and their effect on passivity

Amy C. Lloyd^{a,*}, James J. Noël^a, Stewart McIntyre^b, David W. Shoesmith^a

^a Department of Chemistry, The University of Western Ontario, London, Ont., Canada N6A 5B7

^b Surface Science Western Room G-1, Western Science Centre, The University of Western Ontario, London, Ont., Canada N6A 5B7

Received 9 May 2003; received in revised form 6 January 2004; accepted 6 January 2004

Available online 15 April 2004

Abstract

The passive corrosion properties of a series of Ni–Cr–Mo alloys were investigated. The alloys studied were C22, C2000, C276, C4 and 625. Potentiostatic experiments at potentials within the passive range were obtained as a function of temperature (25–85 °C) for each alloy. Each specimen was subsequently analyzed by time-of-flight secondary ion mass spectrometry (TOF SIMS) and X-ray photoelectron spectroscopy (XPS). Results indicated that much lower passive dissolution currents, and a much slower attainment of steady-state conditions, were observed on those alloys with >20 wt.% Cr content. These alloys also consistently showed only a minor temperature dependence of the passive current. The surface analyses showed that the high-Cr alloys were able to build thicker oxides with a layered structure consisting of an inner Cr–Ni oxide layer and an outer Mo/Cr oxide. By contrast, such a high-Cr content inner layer and structured elemental distribution were not achieved with alloys having a lower bulk Cr content.

For low potentials (200 mV), when Cr dissolution can only occur as Cr(III), additional alloying elements, specifically Mo and W, exert little influence on passive current densities. At 500 mV, a potential at which Cr(VI) release appears to start, the presence of Mo, and especially W, in the outer regions of the oxide suppresses passive dissolution. This may be due to the low dissolution rate of the W-containing surface oxide layer, but some influence of W on the defect density within the oxide cannot be ruled out. The observed temperature dependence for high-Cr alloys (C22, C2000) reflects the lack of steady state and cannot be interpreted as an accurate activation energy.

© 2004 Elsevier Ltd. All rights reserved.

Keywords: Ni–Cr–Mo alloys; Passivity; Corrosion; Point defect model; Anodic polarization

1. Introduction

It is well known that the concentration and distribution of solid-state alloying elements in Ni–Cr–Mo alloys influences their ability to withstand corrosive environments. While the passivation of these alloys is known to be responsible for this corrosion resistance, our understanding of the phenomenon is still incomplete. The goal of this research is to investigate the effects of potential and temperature in an effort to improve our understanding of the features that determine the long-term corrosion durability of industrially manufactured Ni–Cr–Mo alloys. This paper attempts to link the physical and chemical processes occurring during passive corrosion

to compositional and structural changes that occur within the oxide film and alloy surface due to changes in parameters such as temperature and redox condition.

Many studies of passivation and the compositions of passive oxide films have been reported for Ni–Cr and Ni–Cr–Mo alloys [1–3]. These studies, based on results from surface sensitive techniques such as XPS and AES, show that the presence of an inner oxide layer rich in Cr (barrier layer) is a primary factor in enforcing passivity. The exact mechanism by which Mo enhances the corrosion resistance of stainless steels and Ni alloys is less well understood, and a variety of possible mechanisms have been suggested. It has been postulated that Mo on the alloy surface preferentially locates at local defects, which otherwise would act as dissolution sites [4–6], and slows anodic dissolution because of its higher metal–metal bond strength [7,8]. An alternative hypothesis is that MoO_4^{2-} is formed in the solid state in the exterior regions of the film. This MoO_4^{2-} layer is cation selective, and resists the incorporation of anions such as Cl^- and OH^- ,

* Corresponding author. Tel.: +519-661-2111x86248; fax: +519-661-3022.

E-mail addresses: alloyd@uwo.ca (A.C. Lloyd), jjnoel@uwo.ca (J.J. Noël), smcintyr@uwo.ca (S. McIntyre), dwshoesm@uwo.ca (D.W. Shoesmith).

allowing for the growth of a Cr oxide inner barrier layer. The resulting bipolar film stabilizes the oxide phase [9].

This paper investigates the behaviour of Ni–Cr–Mo alloys during potentiostatic polarization as a function of temperature. The first potential, 200 mV_{Ag/AgCl}, was chosen as a representative value for passive conditions. A higher potential of 500 mV_{Ag/AgCl} was chosen to represent the maximum expected extent of ennoblement of these alloys in the presence of aggressive oxidants, e.g. acidic Fe(III) and/or H₂O₂. The highest potential studied was 700 mV_{Ag/AgCl}, chosen as an extreme passive condition just prior to the onset of transpassivity. In a previous paper [10], we described the results for two alloys, C22 and C276. In this work, we present the results for the same series of experiments for an expanded set of alloys including C4, C2000, 625, C22 and C276.

2. Experimental

The alloys used in this study were donated by Haynes International, Kokomo, Indiana. Their compositions are shown in Table 1. Cylindrical samples of 1 cm diameter, with a height of 0.5–1 cm, were cut. A connecting rod of the same material was attached at the back of each sample to allow for an external electrical connection. Each specimen was fixed in an epoxy resin (Dexter Hysol, resin EE4183, hardener HD3561) allowing only a circular face of 0.785 cm² to be exposed to the electrolyte. Each sample was then wet-polished with silicon carbide paper from 180 to 1200 grit finish, ultrasonically cleaned in methanol, and rinsed in ultra-pure deionized water. Samples were subsequently stored in a desiccator at room temperature for 2–3 days prior to experimentation.

A jacketed cell containing a three-electrode configuration was connected to a water circulating thermostatic bath in order to control the temperature of the electrolyte solution to within 1 °C. The cell was placed in a Faraday cage to reduce any outside sources of electrical noise. A 99.95% pure platinum plate was used as the counter electrode, and the reference electrode was an in-house fabricated Ag/AgCl electrode in 0.1 mol L⁻¹ KCl (288 mV versus NHE). All potential values in this paper are reported versus Ag/AgCl unless stated otherwise. The solution used in all experiments was 1.0 mol L⁻¹ NaCl + 0.1 mol L⁻¹ H₂SO₄ prepared us-

ing reagent grade chemicals with ultra-pure deionized water (resistivity of 18 MΩ cm). Solutions were deaerated with ultra-high purity argon gas for 20 min prior to experimentation, and purged continuously throughout the experiment.

All electrochemical measurements were made with a Solartron 1287 potentiostat running Corrware software. Potentiostatic polarization experiments were performed at potentials of 200, 500 and 700 mV. Prior to polarization, the corrosion potential was recorded at 25 °C for 1 h. During polarization, the temperature was raised from 25 to 85 °C in increments applied every 10–12 h. After completion of the electrochemical experiment, each specimen was rinsed in ultra-pure deionized water. The specimens were subsequently analyzed using XPS and TOF SIMS.

Polarization scans were run from –500 to 710 mV and back at a scan rate of 0.02 mV s⁻¹. This was to ensure that the scan reached the highest potential applied during the potentiostatic experiments without progressing into the transpassive region. The potentiostatic polarization experiments described above showed that localized corrosion could occur at the resin–specimen interface. Thus, a resin was not used when recording polarization curves. Instead, the top of the cylindrical electrode and the connecting rod were painted with a protective paint and the electrodes immersed such that the painted portions were not exposed to the solution. Prior to experimentation, the electrodes were prepared by wet-polishing from 180 to 1200 grit with silicon carbide, then with a 1 μm alumina suspension. The electrodes were immediately rinsed in methanol, ultrasonically cleaned in deaerated ultra-pure deionized water for 10 s, then placed into the preheated electrolyte.

All XPS spectra were obtained with a Surface Science Laboratories SSX-100 ESCA spectrometer using monochromatic Al Kα (1486.6 eV) radiation. The binding energy scale was calibrated to give a Au 4f_{7/2} line position at 83.98 eV. Survey spectra were recorded on all samples, followed by high resolution spectra of the Cr 2p and Mo 3d regions. Quantification of the XPS intensities for Cr, Mo and Ni was carried out using Scofield cross-sections and corrections for the inelastic mean free path of the Ni 3p, Cr 3p and Mo 3d photoelectrons were used. Such analyses are believed to be accurate to ±20% [11]. All binding energies reported have an error in the range of ±0.1 eV.

An ION-TOF time-of-flight secondary ion mass spectrometer (TOF SIMS IV) was used to obtain the TOF SIMS depth profiles. A 3 keV Cs⁺ ion beam was used to sputter an area of 500 μm × 500 μm on the specimen and negative secondary ions were collected from a 200 μm × 200 μm area within the sputter crater using a 25 keV monoisotopic ⁶⁹Ga primary beam. The depth scale was quantified using a profilometer to measure the depth of craters through the oxide and metal created by the primary beam. The sputter rate was determined to be 3.2 nm min⁻¹, and is a composite rate for both the oxide and metallic components. Each TOF SIMS profile was calibrated using the exact mass values of at least six known species in a mass spectrum col-

Table 1
Nominal chemical compositions of the alloys studied (wt.%)

Alloying element	625 UNS NO6625	C4 UNS NO6455	C276 UNS N10276	C22 UNS NO6022	C2000 UNS NO6200
Cr	21	16	16	22	23
Mo	9	16	16	13	16
W			4	3	
Fe	5	3	5	3	
Cu					1.6
Ni	62	65	57	56	60

lected during profiling. The ION-TOF has a mass resolution approaching 10,000/200 amu. Since standards to match the complex matrix of an industrially made alloy cannot be obtained, the secondary ion intensities could not be calibrated with any oxide mixtures of known composition. Therefore, the changes observed as a function of depth should be considered as qualitative. Details of the SIMS dual-beam depth profiling method have been reported elsewhere [12].

3. Results

3.1. Electrochemical behaviour—polarization experiments

Polarization curves were recorded at 25 and 60 °C. Those for 60 °C are shown in Fig. 1, and are similar in form to those recorded at 25 °C. All alloys showed a significant suppression of current on the reverse scan from +710 mV, consistent with improved passivity. On the forward scan all alloys sustained cathodic currents until the potential became very positive, i.e., for all alloys except C276, an anodic current was not obtained until the potential equalled or exceeded 250 mV at 25 °C or 400 mV at 60 °C. None of the alloys showed any sign of active behaviour. The more negative corrosion potential (E_{corr}) recorded on the return scan suggests surface oxidation on the anodic scan led to a significant suppression of the cathodic kinetics. Why such an effect should be less marked for C276 than the other alloys is not clear.

3.2. Electrochemical behaviour—potentiostatic experiments

Fig. 2 shows the potentiostatic curves recorded at a potential of 500 mV for all alloys. These plots are representative of the general features observed due to the influence of increasing temperature on all five alloys investigated at each of the three potentials. The current responses were similar for all alloys, each increase in temperature stimulating a rapid current increase followed by decay towards steady state. The initial surge in current was much larger for the low-Cr alloys than it was for the high-Cr alloys.

Fig. 3 shows the current values recorded at the end of the 10–12 h period at each temperature for all alloys. At 200 mV (Fig. 3(a)), all alloys proved immune to localized corrosion throughout the temperature range investigated. For temperatures ≤ 45 °C, the passive current densities for all alloys were very similar, suggesting that the differences in alloy composition are of little significance in determining passive behaviour. With increasing temperature above 45 °C, a clear separation between the high-Cr alloys (>20% Cr; C22, C2000, 625; Table 1) and the low-Cr alloys (14–18% Cr; C276, C4; Table 1) was observed (Fig. 3(a)). The observation of enhanced passivity as Cr content increases is consistent with studies of passivity on Ni–Cr and Ni–Cr–Mo

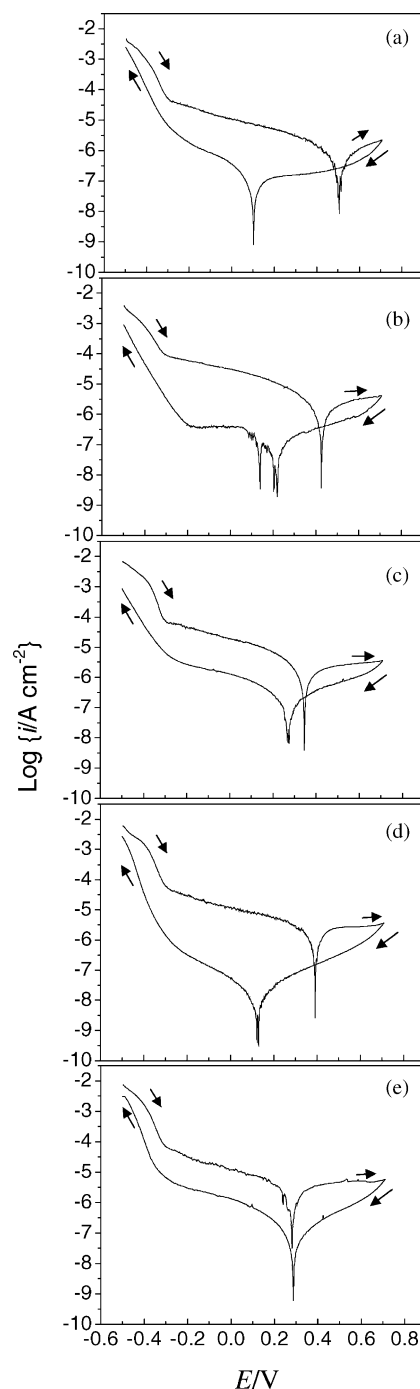


Fig. 1. Polarization scans recorded at 60 °C and 0.02 mV s⁻¹ for (a) C22, (b) C2000, (c) 625, (d) C4 and (e) C276.

alloys [1,3]. The similarities in passive currents for alloys with similar Cr, but various Mo and W, contents indicates that at 200 mV, it is the Cr content that is controlling passive behaviour with the other alloying elements exerting little influence.

At 200 mV, cathodic currents (~ -6 nA cm⁻²) were eventually established on C22 and C2000 at the lower temperatures (Fig. 3(a)). However, caution should be exercised in

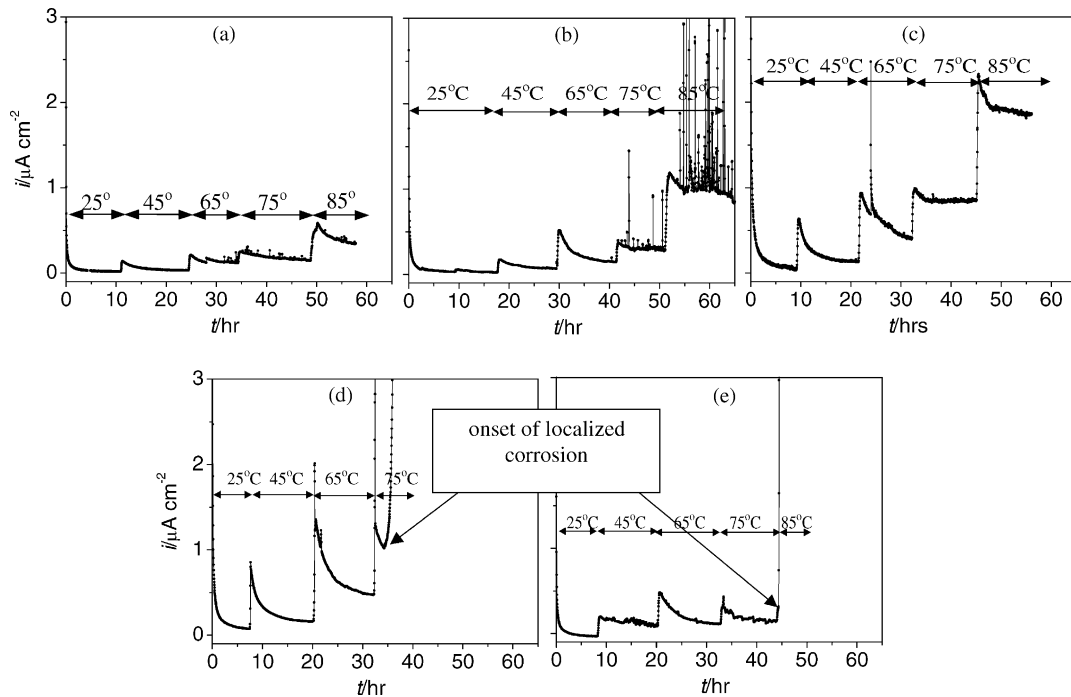


Fig. 2. Current transients recorded on all alloys during polarization at 500 mV for (a) C22, (b) C2000, (c) C276, (d) C4 and (e) 625.

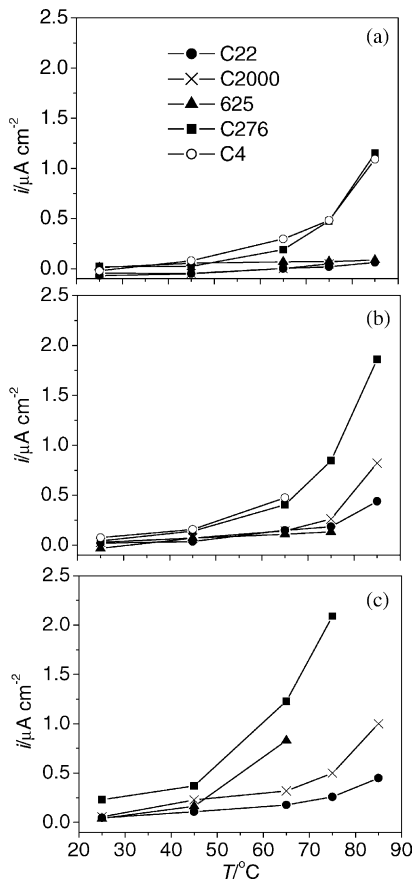


Fig. 3. Current values recorded at the end of each temperature period for all alloys during polarization at (a) 200 mV, (b) 500 mV and (c) 700 mV.

interpreting such small currents. We previously attributed this negative current to the reduction of residual traces of oxygen [13]. While this remains a possibility, the positive E_{corr} values observed in polarization curves suggest that it is also possible that the oxidized surface may have sustained a low rate of proton reduction at 200 mV (Fig. 1).

At 500 mV (Figs. 2 and 3(b)), the passive currents for all alloys exhibited a temperature dependence, although a clear difference between low- and high-Cr alloys remained. The high-Cr alloys exhibited lower currents, a lower dependence of passive current on temperature, and a slower decay in current towards steady state (Fig. 2). A separation in passive currents between C22 and C2000 was observed at 85 °C suggesting an influence of W, present in C22 but not in C2000, on the passive current. At this potential, localized corrosion initiated on C4 and 625 at 75 and 85 °C, respectively. The corrosion was limited to the region of the resin–specimen contact. It is likely that the expansion of the resin with temperature led to its separation from the specimen and the creation of an occluded site, within which a susceptible alloy could initiate crevice corrosion. The tendency to achieve a steady-state passive current over the 10–12 h polarization period can be illustrated with $\log i$ – $\log t$ plots at each temperature (see example, Fig. 4(a)). A value near zero for the slope of such a plot indicates the attainment of a steady-state passive dissolution current. The values recorded at 200 mV were complicated by the switch to cathodic currents, making the slopes of little significance. However, with the exception of the current for 625, those measured at 500 mV are free of such interference and more accurately reflect the film growth and dissolution processes occurring in the passive region.

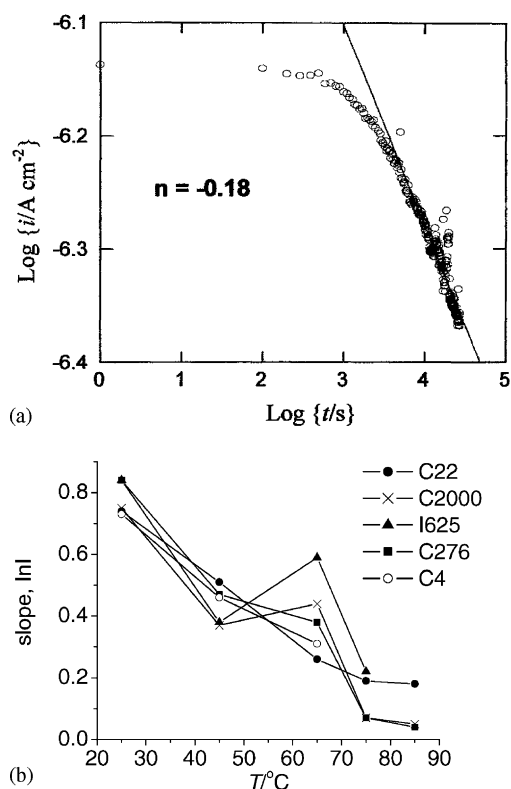


Fig. 4. (a) Representative log–log plot of current transient at 85 °C on C22 during 500 mV polarization and (b) slopes for all alloys at 500 mV as a function of temperature.

As illustrated in Fig. 4(b), the general trend was the same for all alloys; a decreasing slope indicating an increasing trend towards steady state with increasing temperature. Jallerat and Vu Quang [14] observed a similar trend on Ni–Cr–Mo alloys, where, during their first period of polarization, slope values near to or greater than -0.5 , characteristic of a film growth process, were observed. With increasingly aggressive conditions (in their case, more anodic potentials), the slopes tended to zero.

Inspection of the current transients at 500 mV (Fig. 2) shows that an increase in temperature from 45 to 65 °C promoted a more pronounced increase in current than that observed at lower temperatures, and this was followed by a rapid subsequent decay with time. The most likely cause of this behaviour is that the increase in temperature caused a separation of the electrode from the insulating resin. The increased current decay would then have been due to a rapid reaction of the previously unexposed alloy surface. For susceptible alloys, e.g. C4 and 625, this may have led to the onset of crevice corrosion. For those alloys which did not initiate crevice corrosion, this separation led to a slight increase in exposed specimen surface area. While this may have influenced the absolute value of the passive currents somewhat, it does not nullify the differences in observed behaviour between the alloys. What is clear from Fig. 4(b) is that, at the highest temperature achieved, only C22 exhibited a signifi-

cant slope, suggesting that the achievement of steady state would have required a considerable further decrease in the current density. Consequently, the final steady-state passive current for C22 would have been lower than the value plotted in Fig. 3(b), making the difference between this alloy and C2000 even more marked.

At the most noble potential employed (700 mV), the distinction between individual alloys was further blurred, Fig. 3(c), with all alloys showing a substantial increase in current with temperature. Only the two high-Cr and -Mo alloys, C22 and C2000, did not undergo crevice corrosion at the specimen–resin gap. The passive current for C22 was lower than that for C2000 at both 500 and 700 mV, suggesting an influence on the passive current of the 2–4% W, the only significant difference in composition between these alloys. The data for alloy C4 are not shown, as this alloy was not stable above 25 °C, and initiated crevice corrosion at only 45 °C.

3.3. Surface analyses—XPS results

XPS survey spectra detected Ni, Cr, Mo, W, C and O peaks. The air-grown films and those grown at 200 mV on all alloys exhibited strong Ni 2p and Ni 3p lines, indicating the presence of Ni throughout the oxide films. After oxidation at 500 and 700 mV, the Ni 2p peaks were no longer detectable above the background in the survey spectra, while Ni 3p peaks were still observed. This is consistent with the depletion of nickel in the outer regions of the oxide, but its retention within the inner regions of the oxide at these higher potentials. A similar effect was observed by Marcus and co-workers [15,16] on Ni–Cr–Fe alloys in acidic sulphate solutions after polarization at potentials >300 mV versus SHE. High-resolution XPS scans showed that the Cr 2p and Mo 3d peaks were made up of both metallic and oxide components. An example of the fitting performed on the XPS spectra obtained for a sample of C2000 is shown in Fig. 5. All spectra were deconvoluted after a Shirley background correction [17]. The presence of Cr in the 0 and 3+ states is consistent with published literature [16,18]. A metallic Cr peak and the characteristic multiplet splitting for Cr in the 3+ oxidation state (peaks 1–4, Fig. 5(a)) were detected for all alloys. The Cr 2p spectra (Fig. 5(a)) were fit with fixed parameters according to Pratt and McIntyre [19] and recent work by Davidson and Beisinger [20]. Most of the spectra had a characteristic peak for Cr(III) in pure Cr_2O_3 near 577.0 eV; however, for several spectra, this peak was shifted to higher values, between 577.8 and 578.3 eV, suggesting the presence of a hydroxide species. Cr hydroxides have not been as well characterized in the literature, and so, it is difficult to positively assign this peak. In general, all alloys showed an increase in the ratio of Cr(III) to Cr metal with increasing applied potential, and Fig. 6 summarizes the fractions of Cr(III) found on the surface of each alloy as a function of applied potential. The absence of Cr(VI) within the spectra show that any Cr(VI) that may have been pro-

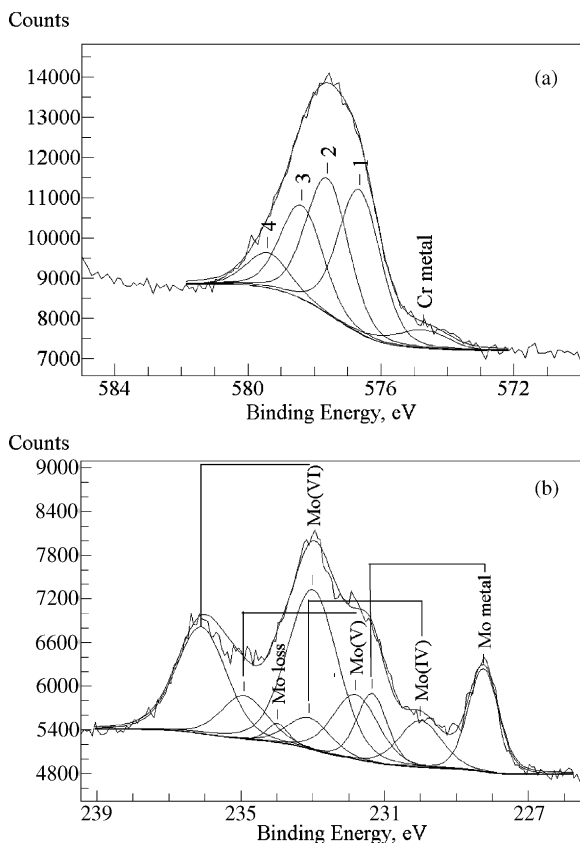


Fig. 5. High resolution scans on C2000 after polarization at 500 mV (a) Cr 2p line and (b) Mo 3d line.

duced at 500 mV and, especially 700 mV, was released to solution.

The Mo 3d spectra were fitted with spin-orbit pair intervals set at 3.1 eV and the parameters outlined by Spevack and McIntyre [21], Fig. 5b. While Mo was present in the oxide in a range of oxidation states (see examples, Fig. 5b and Fig. 7a), the percentage in the Mo(VI) increased substantially with increasing potential for all alloys (Fig. 7b). Alloy C22 appeared to have a lower Mo(VI) content than the other alloys.

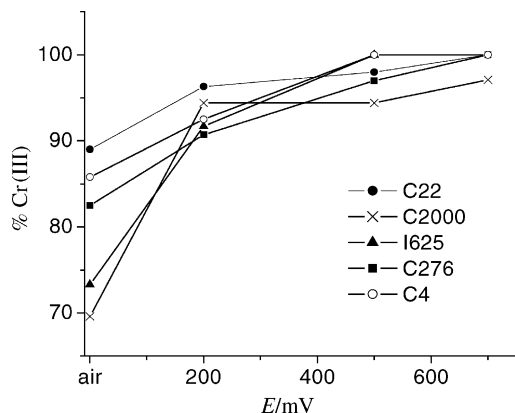


Fig. 6. The percentage of Cr(III) in the Cr 2p spectral line found by deconvolution of the high-resolution scans for all alloys as a function of potential.

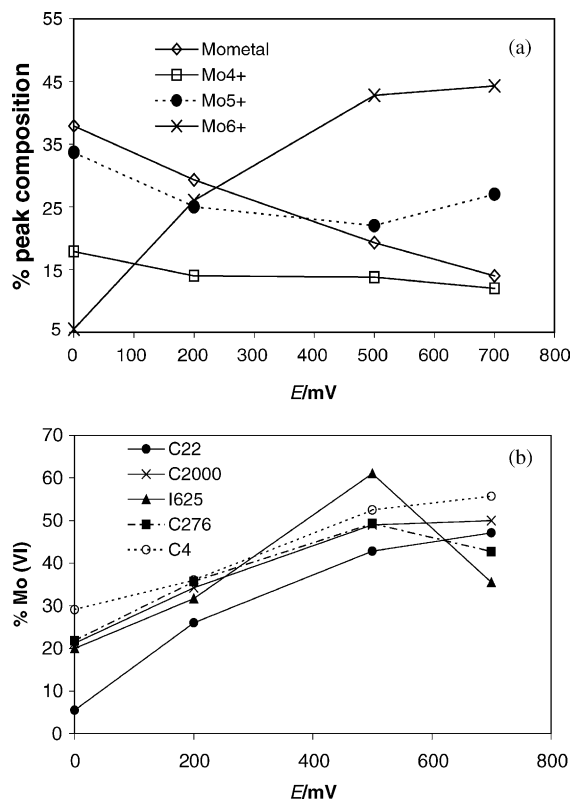


Fig. 7. (a) The distribution of Mo oxides in the Mo 3d line for alloy C22 as a function of potential and (b) the percentage of Mo(VI) in the Mo 3d spectral line as found by deconvolution of the high-resolution scans for all alloys as a function of potential.

The inelastic mean free path for the Ni 3p, Cr 3p and Mo 3d photoelectrons is about 2 nm, and because this was the approximate thickness of the oxide films, quantification of the XPS intensities for Cr, Mo and Ni was carried out using the survey spectra. The oxide layer composition was estimated by considering the ratio of oxidized to unoxidized metal from the high-resolution spectra for each peak (Figs. 6 and 7). As the oxide films on W-containing alloys had less than 1% W at all potentials, W was not included in the estimation of oxide film composition for C22 and C276.

These compositions are noted in Tables 2 and 3 and clearly show the dominant influence of Cr in the oxide. These compositions were used with the oxide film thicknesses, obtained by TOF SIMS, and the bulk densities of the oxides [22] to estimate the approximate charge density associated with the formation of the film (Q_{film} in Tables 2 and 3). The values of the charge passed during anodic oxidation (Q_{exp}) are shown for each alloy and applied potential in Fig. 8. Comparison of these values shows $Q_{\text{film}} \ll Q_{\text{exp}}$, i.e., the currents observed are attributable to anodic film dissolution, not film growth. This conclusion agrees with the results of Krichheim and co-workers [23], who observed that, under stationary conditions, film growth was negligible, and thus the measured current density was equivalent to the dissolution current density. These data also show the much more extensive overall dissolution that occurred on the low-Cr, compared to high-Cr,

Table 2
XPS compositions and calculated charge going to film growth (Q_{film}) for the high-Cr alloys

E (mV)	Oxide layer composition from XPS (at.%)			$Q_{\text{film}}^{\ddagger}$ (mC cm ⁻²)
	NiO	Cr ₂ O ₃	MoO ₃	
C22				
Air	18.6	66.1	15.3	–
200	21.5	68.1	10.4	0.382
500	16.3	70.7	13.0	0.959
700	11.7	70.7	17.6	3.47
C2000				
Air	38.9	47.5	13.6	–
200*	10.0	70.0	20.0	0.386
500	34.3	53.4	12.3	0.750
700	15.9	70.5	13.6	3.26
625				
Air	60.5	30.9	8.60	–
200	23.7	62.1	14.2	0.00
500**	19.0	51.0	30.0	0.00
700***	0	0	100	NA

Where there are values of 0 for Q_{film} , the film was the same thickness or thinner than an air-grown film.

* Note, only taken to 75 °C.

** Corroded at 85 °C.

*** Corroded at 75 °C.

[‡] Corrected for the presence of the air-grown film.

alloys and the widening gap in the extent of dissolution between the W-containing C22 and the W-free C2000 as the applied potential was increased (Fig. 8).

3.4. Surface analyses—TOF SIMS results

TOF SIMS profiles were recorded for all alloys after 2 days of air exposure and on completion of every experiment

Table 3
XPS compositions and calculated charge going to film growth (Q_{film}) for the low-Cr alloys

E (mV)	Oxide layer composition from XPS (at.%)			$Q_{\text{film}}^{\ddagger}$ (mC cm ⁻²)
	NiO	Cr ₂ O ₃	MoO ₃	
C276				
Air	31.3	59.0	9.70	–
200	36.3	39.8	23.9	0.186
500	23.8	48.9	27.3	0.378
700*	9.70	70.0	20.3	1.93
C4				
Air	22.8	65.6	11.6	–
200	12.2	74.0	13.8	0.00
500**	12.8	66.7	20.5	0.00
700***	9.60	71.1	19.3	3.86

Where there are values of 0 for Q_{film} , the film was the same thickness or thinner than an air-grown film.

* Corroded at 85 °C.

** Corroded at 75 °C.

*** Corroded at 65 °C.

[‡] Corrected for the presence of the air-grown film.

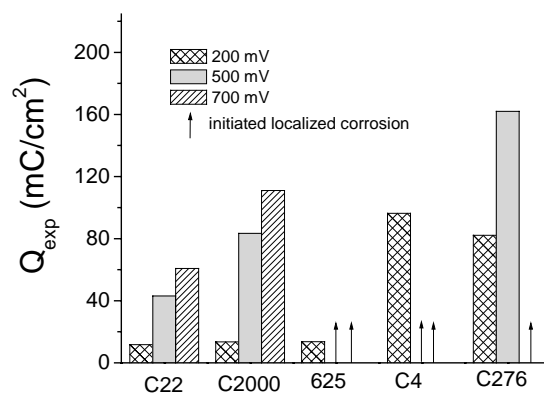


Fig. 8. Calculated values of charge passed during polarization (Q_{exp}) at each potential for all alloys.

at each of the three potentials studied. Figs. 9 and 10 show the profiles obtained at 200 and 500 mV, respectively. While an absolute quantification of elemental composition may be unachievable by this technique, the relative concentrations of various elements can be determined providing it is assumed that the sputtering efficiencies of the various oxide components are the same from alloy to alloy. Such a comparative analysis is made in Figs. 11 and 12, which show the Cr/Mo ratios throughout the oxides for each alloy after each treatment. The ratios are grouped according to potential (Fig. 11) and for each alloy (Fig. 12). The plots for each alloy in these figures extend to the thickness of the oxide layer, estimated by measuring from 0 nm to the inner edge of the deepest peak at half the height. Also, the data recorded for the outer 0.1–0.2 nm of the surface were not included since ratios were not necessarily accurate due to the small measured intensities. The oxide film thicknesses are summarized in Fig. 13.

Based on the Cr/Mo ratios, there is a clear difference in air-oxidation behaviour between the three high-Cr alloys (625, C22 and C2000) and the two low-Cr alloys (Fig. 11(a)). The increasing Cr/Mo ratio from the outer to the inner regions of the film for the high-Cr alloys indicates the tendency for these alloys to form a Cr-rich inner layer, a feature not observed for the low-Cr alloys, which show an almost negligible tendency to segregate Cr and Mo. The larger ratio obtained for 625 compared to C22 and C2000 reflects the larger Cr/Mo ratio in the bulk of this alloy (Table 1). Also, the TOF SIMS signal for Ni in the oxide and the Ni content of the oxide measured by XPS; Table 2 shows the air-grown oxide on this alloy to be dominated by its Ni content.

The TOF SIMS profiles taken after treatment at 200 mV (Fig. 9) were not substantially different to those recorded after air oxidation, showing the minimal effect of anodic polarization at this potential. The Cr/Mo ratios in Fig. 12 show a measurable but minor increase in Cr/Mo segregation at 200 mV from the air-grown films for the high-Cr alloys. This increase is exaggerated for 625, but again, it is likely only a result of the low bulk Mo content, which becomes emphasized under polarization conditions. For the

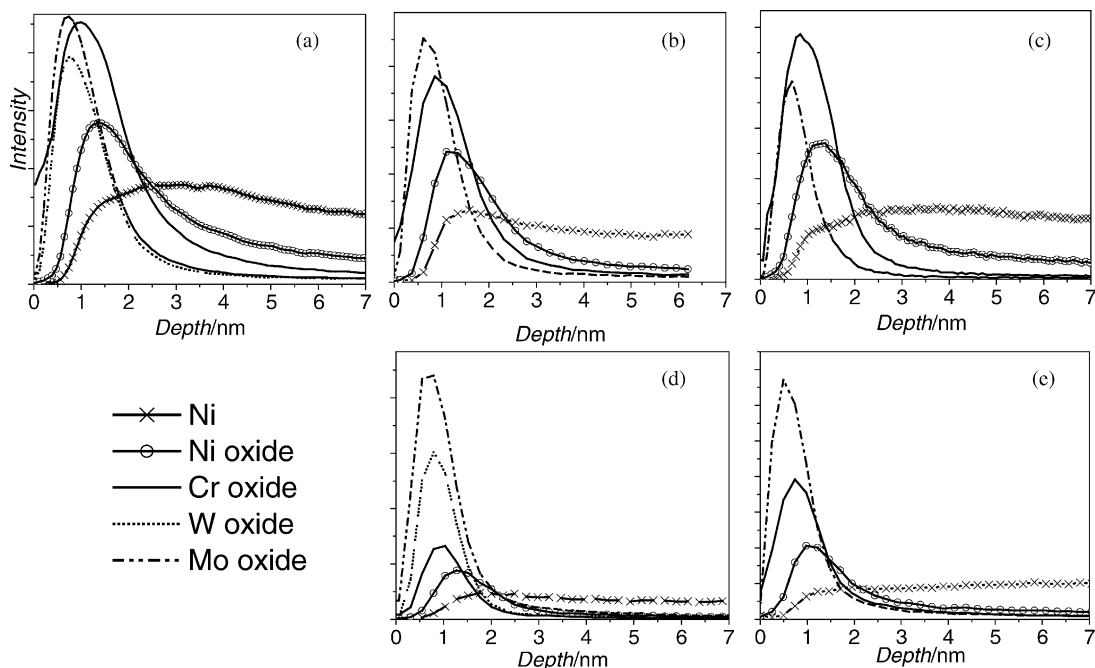


Fig. 9. TOF SIMS depth profiles after treatment at 200 mV for (a) C22, (b) C2000, (c) 625, (d) C276 and (e) C4.

high-Cr-containing alloys, it was observed (Fig. 9(a–c)), that there was also a significant signal for Cr at the outer edges of the film. Fig. 8 shows that the extent of dissolution at 200 mV is the same for these three alloys. This is consistent with Cr, as opposed to other alloying elements, being the dominant cation influencing passive dissolution at this potential.

The TOF SIMS profiles for the lower Cr alloys do not show an enhancement of Cr at the oxide–solution interface (Fig. 9(d) and (e)) and no tendency to segregate Cr and

Mo to the inner and outer regions of the film, respectively, as observed for the high-Cr alloys. This inability to form a Cr-enriched inner layer correlates with the much higher extents of anodic dissolution observed for the low-Cr alloys (C4 and C276) (Fig. 8).

Compared to the low-Cr alloys, there was a noticeable enrichment of Ni in the outer surface of the high-Cr alloys (Fig. 9). The observation of both Ni 2p and Ni 3p signals in the XPS spectra confirms that a general distribution of Ni persisted in the oxide. Such an increased Ni content in

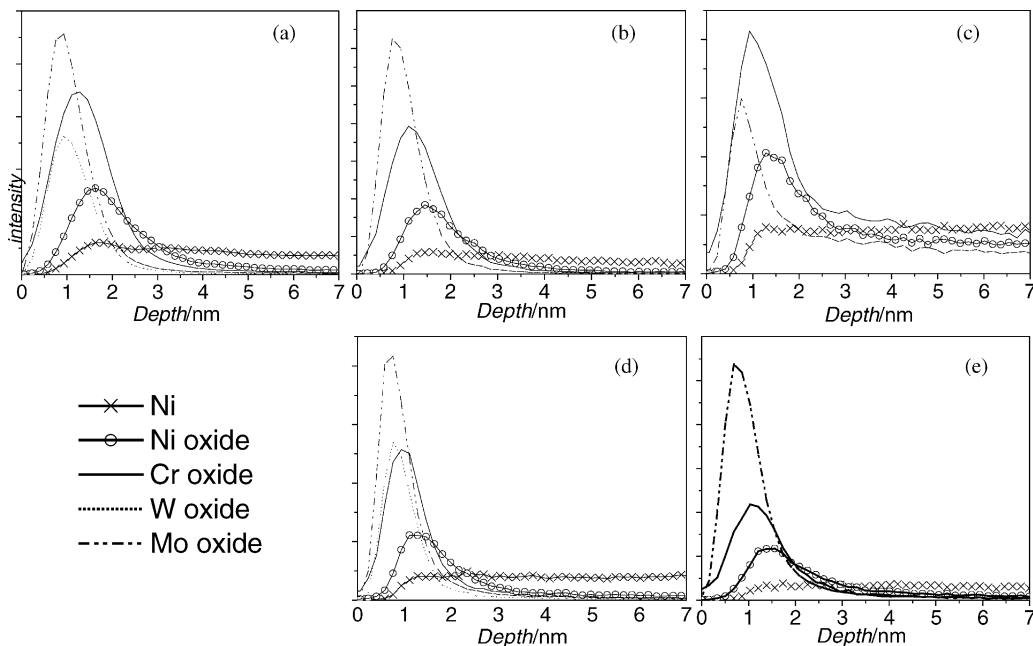


Fig. 10. TOF SIMS depth profiles after treatment at 500 mV for (a) C22, (b) C2000, (c) 625, (d) C276 and (e) C4.

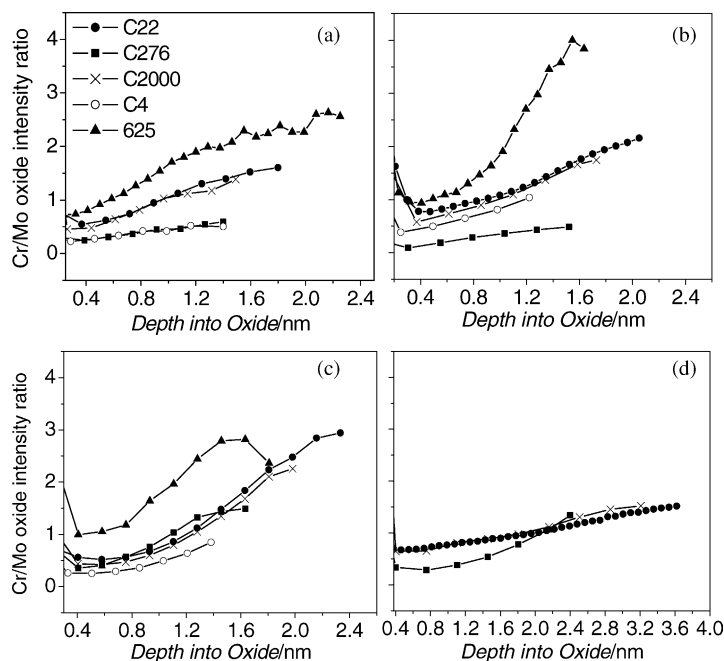


Fig. 11. Cr/Mo intensity ratios from TOF SIMS depth profiles for all alloys for (a) air-grown films, (b) after treatment at 200 mV, (c) at 500 mV and (d) at 700 mV. The data are terminated at the thickness of the oxide for each alloy.

the surface of the alloy was reported by Maurice et al. [16] for Fe–Cr–Ni alloys (Cr 18–22%) and by Jabs et al. [2] for Ni–Cr alloys with either 20% or 34% Cr. According to Maurice et al. [16], this enrichment slows down the formation of the Cr oxide inner layer. This would be consistent with our observation of very low, and even negative, passive current densities and very low Q_{exp} values (Fig. 8) measured on these alloys at 200 mV.

No similar enrichment was observed for the low-Cr-containing alloys (C276 and C4) (Fig. 9). Much larger passive currents (Fig. 3(a)) and dissolution charges (Q_{exp}) (Fig. 8) were observed for these two alloys at 200 mV. This suggests that a more extensive dissolution of Ni occurred.

The disappearance of the Ni 2p peak from the XPS spectra, but the survival of the Ni 3p peak, after polarization at 500 mV, suggests the leaching of Ni from the outer regions of the oxide but its retention in the inner regions. This is consistent with TOF SIMS profiles at 500 mV (Fig. 10), which show the persistence of Ni only within the inner regions of the film. These TOF SIMS profiles also show that, for alloys C22 and C2000, there was an enhanced relative segregation of Cr to the inner film region and of Mo to the outer film region compared to electrodes polarized to 200 mV. This is most clearly shown in the Cr/Mo ratios (plotted in Figs. 11(c), 12(a) and (b)). Also, any Cr signal observed in the outermost regions of the oxide films at 200 mV was no longer present at 500 mV, suggesting some minor dissolution of Cr, as Cr(VI), may have been possible at this potential.

Considering the anticipated rapid leaching of the Ni under anodic conditions, its retention along with Cr, in the inner regions of the oxide suggests the presence of a stable nickel chromite layer. Nickel chromium ferrites

($\text{Ni}_{0.6}\text{Cr}_x\text{Fe}_{2.4-x}\text{O}_4$) with a high value of x (>1.0) have been shown to have extremely low dissolution rates even in aggressive chelating solutions at temperatures up to 140 °C [24]. By analogy, similarly low dissolution rates would be expected for nickel chromites. Also, Schmuki et al. [25] have shown that the incorporation of Fe into chromium oxide suppresses the anodic dissolution current for these oxides, and we would expect a similar, or even enhanced, suppression for Ni substitution in chromium oxides. The XPS data in Tables 2 and 3 suggest that the Ni content of this layer could have been in the 16–35% range.

By contrast, the low-Cr alloys showed a much less pronounced retention of Cr and Ni together (without the presence of Mo) in the inner oxide layer (Figs. 9 and 10). Some degree of Cr/Mo segregation was observed for C276, which remained passive at 500 mV, but not for C4, which suffered crevice corrosion. The TOF SIMS profiles in Figs. 9 and 10, also clearly show that W segregated to the outer regions of the film with Mo. A close inspection of Figs. 11 and 12 shows that the Cr/Mo ratios for C22 and C2000 were effectively equal at equivalent depths within the oxide and the primary difference was that the oxide on C22 grew thicker at all potentials than that on C2000. For the high-Cr alloys in general, not only was segregation of Cr to the inner regions of the oxide more marked, but the films achieved a greater overall thickness (Fig. 13).

Shown in Fig. 14(a) and (b), is the relationship between passive current densities at 500 mV for the C-series alloys (all alloys except 625) and the Cr/Mo ratio at the oxide film/alloy boundary and the oxide film thickness, respectively. The relationship between oxide thickness and Cr/Mo ratio clearly indicates the interdependence of these two fea-

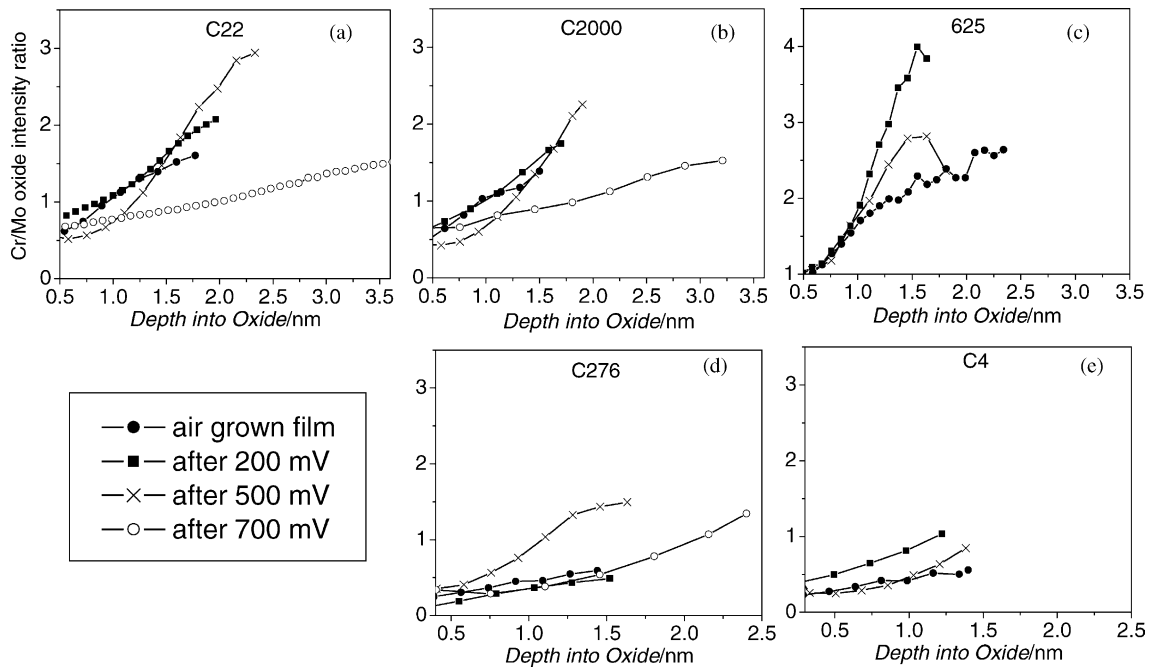


Fig. 12. Cr/Mo intensity ratios from TOF SIMS depth profiles after treatment at each potential for (a) C22, (b) C2000, (c) 625, (d) C276 and (e) C4.

tures, Fig. 15. While there were effectively no differences in passive current densities at 200 mV between alloys whose compositions differ only in W content (i.e., C276 and C4 or C22 and C2000), Figs. 3b and 14 show that there is an obvious effect of W at 500 mV. The presence of W in C276 and C22 appears to have suppressed the passive current, and to have enhanced the film thickness and degree of Cr/Mo segregation compared to their counterparts, C4 and C2000. It should be noted that the oxide film thickness, and possibly also the Cr/Mo ratio for C22, were underestimated in this comparison, since the passive current value was not recorded under steady-state conditions (Fig. 4), and would eventually have achieved a lower value.

Although the TOF SIMS profiles for the alloys treated at 700 mV are not shown, the Cr/Mo ratios for those alloys that remained passive at this potential are shown in Fig. 11(d).

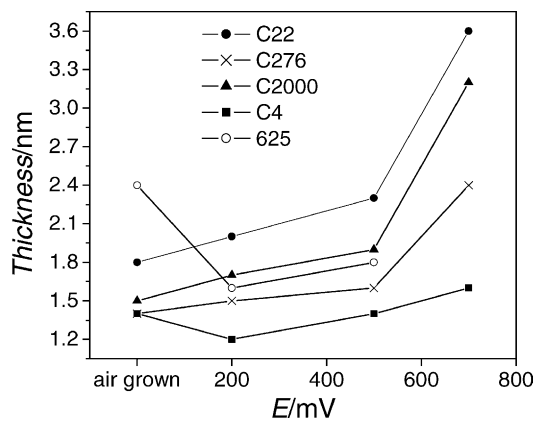


Fig. 13. Oxide thickness for all alloys as a function of potential.

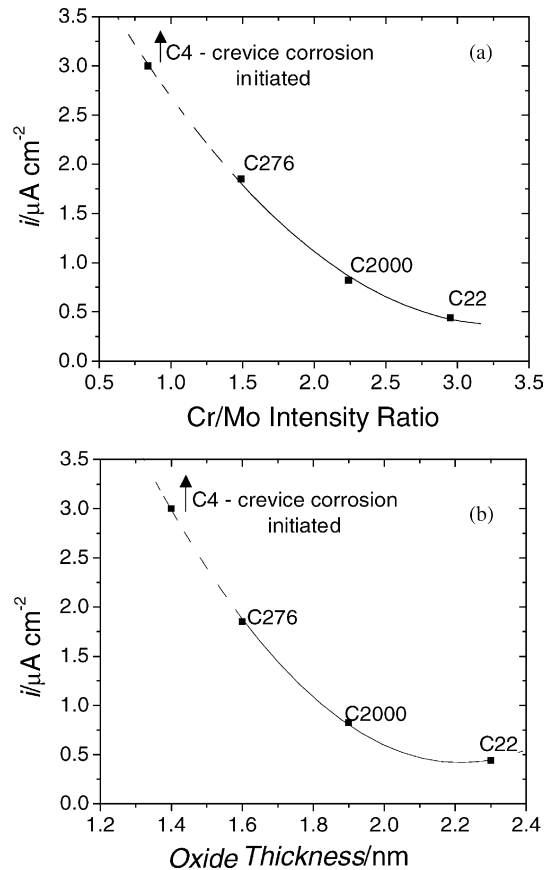


Fig. 14. (a) The effect of the Cr barrier layer on the final current density measured at 500 mV, 85 °C and (b) the effect of oxide thickness on current density measured at 500 mV, 85 °C.

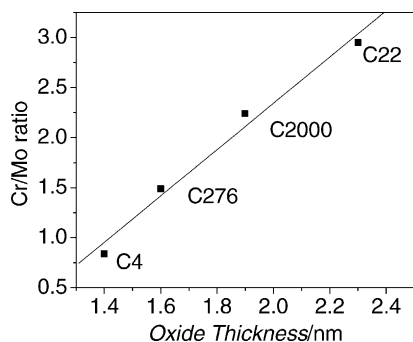


Fig. 15. The relationship between the oxide thickness and the Cr inner barrier layer.

This figure clearly shows that the Cr/Mo segregation was lost, even though the absolute Cr content of the oxide remained high, or even increased (Tables 2 and 3). Comparison of the behaviours of C22 and C2000 (Fig. 3(c)) shows that, at this more noble potential, the differences in passive current density became apparent at temperatures as low as 45 °C. This suggests that once Cr oxidation and release becomes possible, the W content of the alloy plays a more significant role in suppressing passive dissolution. A similar comparison between C276 and C4 was not possible at this potential since C4 underwent crevice corrosion at only 45 °C.

4. Discussion

The point defect model (PDM) [26] can provide a framework for the interpretation of these results. This model was developed to describe the processes involved in the growth and dissolution of bilayer passive films consisting of a compact inner (barrier) layer at the oxide–alloy interface covered by an outer (porous) layer at the oxide–solution interface. Fig. 16 shows a schematic representation of the physico-chemical processes that occur during film growth and dissolution according to this model. During film growth, cation vacancies (V_m) are generated at the barrier layer–outer layer interface (4 in Fig. 16) and consumed at the alloy–barrier layer interface (1 in Fig. 16). Likewise, anion vacancies ($V_o^{\bullet\bullet}$) are formed at the alloy–barrier layer interface (2 in Fig. 16) and consumed at the barrier layer–outer layer interface (5 in Fig. 16). The fluxes of cation and anion vacancies are in the directions indicated (8 and 9, respectively, in Fig. 16), and although the transfer of cations from the oxide to the solution is shown as an electrochemical process (4 and 6 in Fig. 16), it could also be a chemical dissolution involving the transfer to solution of a cation without a change in oxidation state (7 in Fig. 16).

A key feature of the PDM is that the field within the growing oxide does not change with oxide thickness. The current decays with time as the potential drop across the alloy–barrier layer interface decreases. This leads to a de-

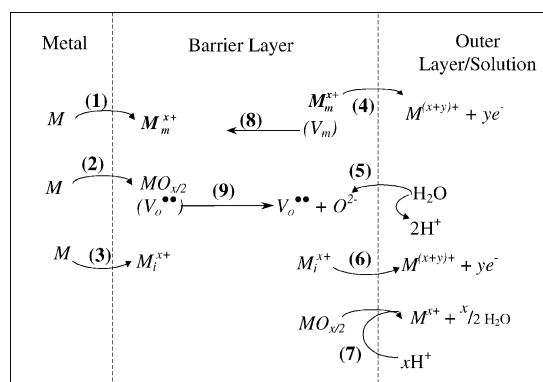


Fig. 16. Description of the point defect model: (1) injection of lattice cation with elimination of a cation vacancy, (2) injection of lattice cation accompanied by creation of an oxygen vacancy, (3) creation of an interstitial cation, (4) oxidative dissolution and creation of a cation vacancy, (5) elimination of an oxygen vacancy, (6) oxidative dissolution of an interstitial cation, (7) chemical oxide dissolution, (8) transport of cation vacancies and (9) transport of anion vacancies.

crease in the rate of injection of cations from the metal into the film, and in the rate of generation of oxygen vacancies. The rate controlling process during film growth is charge injection into the film at the alloy–film interface, and film growth continues until the rate of growth equals the rate of film dissolution. Thus, once steady state is achieved, rate control must be via the rate of the dissolution process, and we would expect the temperature dependence of the current to reflect the activated state of the oxide dissolution step. By contrast, if steady state is not achieved, then the temperature dependence of the current would be determined by the rate of defect injection and how it was changing as the oxide thickened. The number density of defects in the oxide would then determine the oxide dissolution rate. This is consistent with studies on the dissolution kinetics of oxide powders, which show a clear correlation between dissolution rate and defect density [27].

Our observation that the Cr content is the key feature causing the differences in passive currents between the alloys is consistent with the available data on the Cr content of oxides on Fe–Cr alloys [28,29], which show that the cationic fraction of Cr in the passive layer increases dramatically with alloy Cr content in the range 13–20%. Since considerable published evidence exists to show that passive currents decrease with an increase in alloy Cr content [30], our observations of lower passive currents for the high-Cr (C22, C2000, 625) as opposed to low-Cr (C276, C4), alloys are not unexpected.

At 200 mV, the dominance of the influence of Cr is expected since Cr(III) should be stable at this potential, and the steady-state current should be determined by the balance between defect creation at the alloy–oxide interface (determined by the rate of reaction 2, Fig. 16) and chemical oxide dissolution (determined by the rate of reaction 7, Fig. 16). An important difference between the high- and low-Cr oxides is the ability of the high-Cr alloys to segregate

Cr to the alloy–oxide interface on air exposure. This means that, on immersion, the concentration of Cr (and Ni) at the alloy–oxide interface, which appears to be a critical feature in achieving low passive current densities, is already established. Subsequent polarization at 200 mV enhances this segregation process (Cr and Ni to the inner oxide region, Mo (and W) to the outer oxide region) and a very large difference in passive current densities between the high- and low-Cr alloys ensues (Fig. 3(a)).

An increase in applied potential to 500 mV increases the passive current densities on all alloys, and enhances the Cr–Ni, Mo–W segregation in the oxide. This segregation process, which yields a bipolar film structure, is consistent with observations made on Mo-containing stainless steels [31,32]. It has been claimed that the Mo(VI) in the outer layers of the oxide is stabilized as MoO_4^{2-} by the high electric field, a process that leads to the deprotonation of OH^- within the film. This supplies O^{2-} , which enhances the formation of a protective Cr_2O_3 inner layer.

Of key importance at this potential is the observation that effectively all the current is going to dissolution processes and that those alloys which achieve a low passive current density (C22 and C2000) not only have an increase in the extent of Cr–Ni, Mo–W segregation, but also thicken, whereas the oxide films on lower Cr alloys which, have either a higher passive current (C276) or undergo crevice corrosion (C4) neither significantly improve the extent of segregation nor thicken substantially.

An increase in oxide thickness leading to a decrease in passive current density is expected, based on the PDM. However, since the composition and structure of the passive film also change considerably from 200 to 500 mV, it is likely that the field in the oxide also changes with potential, and also with time at a constant potential. These claims are supported by the observations that Cr–Ni, Mo–W segregation and oxide thickening occur simultaneously on alloys with low passive currents (C2000, C22) and a slow approach to steady state (C22), but not on the others. Presently, this is not a feature in the PDM.

Such a claim is consistent with the observations of Bojinov et al. [33,34] who showed that the resistance of the oxide (on Ni–20Cr, Ni–15Cr; alloy 600 and C276) increased by many orders of magnitude over the potential range 200–500 mV versus SHE (on our Ag/AgCl potential scale), as expected for a combination of oxide thickening and a decrease in defect density in the oxide as the inner Cr–Ni layer forms and anneals. A similar defect annealing process has been demonstrated by Yang et al. [18] for prolonged potentiostatic treatment of Fe–17Cr. A similar defect annealing process, without an accompanying change in oxide composition, has been observed for titanium [35].

At potentials of 200 mV, there appears to be no influence of the alloying elements Mo and W on the passive current densities. However, at 500 mV, the influence of W in

suppressing the passive current density of C22 to a lower value than that of C2000 is apparent. Bojinov et al. [34] also showed a decrease in passive current in the W-containing C276 compared to alloys of otherwise similar composition, Alloy 600 and Ni–15Cr. Although not discussed in their paper, the differences in alloy behaviour at the two potentials appears to be in the nature of the dissolution process that balances the rate of defect injection at the alloy–oxide interface. At 500 mV, the anodic dissolution of Cr as CrO_4^{2-} , while only a minor process, appears possible, whereas at 200 mV, only chemical dissolution is feasible. Oxidative dissolution would lead to the introduction of a metal vacancy (4 in Fig. 16) and an increase in passive current. Once the Cr stability within the film becomes threatened, e.g. by a higher potential or temperature, then the influence of Mo and, especially, W in suppressing the passive current appears to increase.

In its segregation behaviour within the oxide film, W behaves identically to Mo and is predominantly located in the outer regions of the film. This suggests a common role for both elements. However, the solubility of W in acidic solutions is 2–3 orders of magnitude lower than that for Mo [36] and the dissolution rate of a W-enriched oxide surface would be expected to be lower than one simply enriched in Mo. As a consequence, the steady-state passive dissolution condition would be expected to occur at a lower current density when W is present. A suppression of film dissolution rate would lead also to a greater steady-state oxide film thickness, as observed for C22 compared to the W-free C2000.

This straightforward effect on oxide dissolution rate may not be sufficient to explain totally influence of W (and, by inference, the influence of the similar Mo) on passive dissolution. Our XPS analyses show the W content of the oxide to be <1%, making it difficult to imagine that it could suppress dissolution so markedly. An influence on the mobility of cation defects in the oxide film, as proposed for Mo by Macdonald and Urquidi-Macdonald [26,37], may also be important. That such a mechanism may be operative is suggested by our observation that an influence of W is only observed once the injection of cation vacancies into the oxide, as a consequence of Cr(III) to Cr(VI) oxidation, occurs at 500 mV.

Although the primary focus of this study has not been localized corrosion, a few comments are merited. Besides reinforcing the protectiveness of the high-Cr-containing barrier layer, it is claimed that MoO_4^{2-} gives the outer regions of the oxide a cation selective character [38], thereby discriminating against the incorporation of Cl^- into the passive film and preventing its breakdown to initiate localized corrosion. In our previous paper, comparing C22 and C276 [10], we claimed that the Cr content of the alloy was the critical feature that enabled the passive film to resist breakdown. However, the studies from this wider range of materials indicate a clear role for Mo and W. Thus, despite the high-Cr content and low passive current values, 625 rapidly failed

by crevice corrosion for $T = 65^\circ\text{C}$, and the only two alloys to resist this process throughout the whole experimental sequence were the high-Cr/high-Mo–W alloys C22 and C2000. Of the two low-Cr alloys, C276 containing W, was clearly superior to C4.

5. Summary and conclusions

The responses of a series of Ni–Cr–Mo alloys to changes in applied potential and temperature have been investigated in chloride/sulphate solutions of pH 1. The passive current densities measured for the high-Cr alloys (C22, C2000 and 625) are significantly lower than those measured for the low-Cr alloys (C4 and C276). This can be attributed to a combination of the higher Cr content and the ability to segregate Cr–Ni to the alloy–oxide interface and Mo–W to the oxide–solution interface.

This ability to segregate the alloy components within the oxide is coupled to an increase in oxide thickness with applied potential. For low potentials (200 mV), when Cr in the oxide is stable in the +3 oxidation state, the alloy Cr content is the dominant property leading to low passive currents.

For higher potentials (500 mV), at which Cr(III) oxidation to Cr(VI) becomes possible, the presence of Mo, and particularly W, in the outer regions of the oxide becomes important in maintaining low passive currents. The ability of Mo and W to suppress passive currents is maintained at a potential of 700 mV, the threshold for the onset of transpassive dissolution, even though the segregation of Ni–Cr and Mo–W is lost. The importance of Mo–W in suppressing localized corrosion was clearly seen in the case of 625 which, despite a high-Cr content, experienced crevice corrosion at 65°C , whereas C22 (with Mo and W) and C2000 (with Mo only) did not.

Acknowledgements

Haynes International, Kokomo, Indiana, for their generous donation of material. This project received funding from the National Science and Engineering Research Council of Canada (NSERC).

Appendix A. Nomenclature

M	metal atom
M_i^{x+}	metal cation in interstitial site
M_m^{x+}	metal cation in cation site
$\text{MO}_{x/2}$	oxide
V_m	cation vacancy
$V_o^{\bullet\bullet}$	anion vacancy

References

- [1] S. Boudin, J.-L. Vignes, G. Lorang, M. Da Cunha Belo, G. Blondiaux, S.M. Mikhailov, J.P. Jacobs, H.H. Brongersma, *Surf. Interface Anal.* 22 (1994) 462.
- [2] T. Jabs, P. Borthen, H.-H. Strehblow, *J. Electrochem. Soc.* 144 (4) (1997) 1231.
- [3] G. Lorang, N. Jallerat, K. Vu Quang, J.-P. Langeron, *Surf. Interface Anal.* 16 (1990) 325.
- [4] R.S. Lillard, M.P. Jurinski, J.R. Scully, *Corrosion* 50 (1994) 251.
- [5] R.C. Newman, *Corros. Sci.* 25 (1985) 331.
- [6] R.C. Newman, *Corros. Sci.* 25 (1985) 341.
- [7] P. Marcus, V. Maurice, in: M. Schutze (Ed.), *Corrosion and Environmental Degradation*, Wiley-VCH, New York, 2000 (Chapter 3).
- [8] P. Marcus, *Corros. Sci.* 36 (12) (1994) 2155.
- [9] C.R. Clayton, Y.C. Lu, *J. Electrochem. Soc.* 133 (12) (1986) 2465.
- [10] A.C. Lloyd, D.W. Shoesmith, N.S. McIntyre, J.J. Noël, *J. Electrochem. Soc.* 150 (4) (2003) B120.
- [11] D. Briggs, M.P. Seah, *Practical Surface Analysis by Auger and Photoelectron Spectroscopy*, Wiley, Toronto, ON, 1983.
- [12] K. Iltgen, C. Bendel, A. Benninghoven, *J. Vac. Sci. Technol. A* 15 (3) (1997) 460.
- [13] D.S. Dunn, C.S. Brossia, O. Pensado, in: *Corrosion 2000*, Paper No. 01125 NACE International, Houston, TX, 2000.
- [14] N. Jallerat, K. Vu Quang, *Corros. Sci.* 31 (1990) 539.
- [15] P. Marcus, J.M. Grimal, *Corros. Sci.* 33 (5) (1992) 805.
- [16] V. Maurice, W.P. Yang, P. Marcus, *J. Electrochem. Soc.* 145 (3) (1998) 909.
- [17] D.A. Shirley, *Phys. Rev. B* 5 (12) (1972) 4709.
- [18] W.P. Yang, D. Costa, P. Marcus, *J. Electrochem. Soc.* 141 (1) (1994) 111.
- [19] A.R. Pratt, N.S. McIntyre, *Surf. Interface Anal.* 24 (1996) 529.
- [20] R. Davidson, M. Beisinger, Private Communication, Surface Science Western, University of Western Ontario, February 2003.
- [21] P.A. Spevack, N.S. McIntyre, *J. Phys. Chem.* 97 (1993) 11020.
- [22] R.C. Weast (Ed.), *Handbook of Chemistry and Physics*, 49th ed., Section B, CRC, OH, 1971.
- [23] B. Heine, R. Krichheim, *Corros. Sci.* 31 (1990) 533.
- [24] R.M. Sellers, W.J. Williams, *Faraday Discuss. Chem. Soc.* 77 (1984) 265.
- [25] P. Schmuki, S. Virtanen, H.S. Isaacs, M.P. Ryan, A.J. Davenport, H. Bohni, T. Stenborg, *J. Electrochem. Soc.* 145 (3) (1998) 791.
- [26] D.D. Macdonald, *Pure Appl. Chem.* 71 (1999) 951.
- [27] R.L. Segall, R.St.C. Smart, P.S. Turner, *Surface and New Surface Chemistry of Oxide Materials*, Elsevier, Amsterdam, 1988 (Chapter 13).
- [28] K. Osozawa, H.J. Engell, *Corros. Sci.* 6 (8) (1966) 389.
- [29] K. Asami, K. Hashimoto, S. Shimodaira, *Corros. Sci.* 18 (1978) 551.
- [30] P. Schmuki, *J. Solid State Electrochem.* 6 (3) (2002) 145.
- [31] I. Oleffjord, L. Wegrelius, *Corros. Sci.* 31 (1990) 89.
- [32] A. Schneider, D. Kuron, S. Hoffman, R. Kirchheim, *Corros. Sci.* 31 (1990) 191.
- [33] M. Bojinov, G. Fabricins, P. Kinnunen, T. Laitenen, K. Makela, T. Soario, G. Sundholm, *Electrochim. Acta* 45 (2000) 2791.
- [34] M. Bojinov, G. Fabricins, P. Kinnunen, T. Laitenen, K. Makela, T. Soario, G. Sundholm, K. Yliniemi, *Electrochim. Acta* 47 (11) (2002) 1697.
- [35] K. Leitner, J.W. Schultze, U. Stimming, *J. Electrochem. Soc.* 133 (1986) 1561.
- [36] C.F. Daes, R.E. Mesmer, *The Hydrolysis of Cations*, Wiley-Interscience, New York, 1976 (Chapter 11).
- [37] M. Urquidi-Macdonald, D.D. Macdonald, *J. Electrochem. Soc.* 134 (1) (1987) 41.
- [38] B. MacDougall, *J. Electrochem. Soc.* 130 (1) (1983) 114.